Hierarchical transformations in sound envelope encoding differ across cortical layers

Chase A. Mackey[1], and Yoshinao Kajikawa[1,2]

1. Nathan Kline Institute for Psychiatric Research, Center for Biomedical Imaging and Neuromodulation, Orangeburg, NY 10962

2. New York University School of Medicine, Department of Psychiatry, New York, NY 10016

Corresponding authors: chase.mackey@nki.rfmh.org; yoshinao.kajikawa@nki.rfmh.org

Address: 140 Old Orangeburg Rd., Orangeburg NY, 10962

The authors declare no conflicts of interest

Acknowledgements

Funding sources: R01DC015780, R01DC012947 and R01DC019979.

The authors thank Dr. Monica N. O'Connell for helpful comments on an earlier version of the manuscript.

Abstract

Amplitude-modulation (AM) is critical for the perception of complex sounds, and transformations in AM encoding may underlie primate-specific aspects of complex sound perception. The nonhuman primate model provides an opportunity to understand what circuit mechanisms generate hierarchical and interhemispheric transformations of AM encoding in different circuits across the cortical hierarchy. To address this, here we report the encoding of AM signals as a function of cortical layer and hemisphere in primary area A1 and the tertiary parabelt (PB) area of five NHPs. We presented AM noise and click trains to awake NHPs while recording from linear array multielectrodes straddling cortical layers. A1 typically encoded all AM frequencies (1.6-200 Hz) with high (> 90%) classification accuracy, while the PB encoded lower (~1.6-25 Hz) frequencies. The granular and infragranular layers displayed enhanced AM

encoding relative to the supragranular layers in A1, but this deep-layer enhancement was reduced in the PB. Both areas displayed enhanced AM encoding in the left hemisphere, restricted to the supragranular layers. These results represent the first analysis of AM encoding in the PB, in which we identify circuits differ in their temporal sensitivity across the hierarchy, and suggest local supragranular neuronal populations contribute to hemispheric specialization.

Introduction

Sound envelope fluctuations are a key sound feature that drives the perception of complex stimuli such as species-specific vocalizations and music (Ding et al., 2017; Henry et al., 2017; Rosen, 1992). Many previous studies have gained insight into how sound envelope encoding differs across the auditory pathway by recording neuronal responses to click trains and sinusoidally amplitude modulated (AM) tones and noise in nonhuman animals (Henry et al., 2016; Joris and Yin, 1992; Joris et al., 2004; Langner and Schreiner, 1988; Mackey et al., 2024a; Nelson and Carney, 2007; Rhode et al., 2010; Wang et al., 2008). These studies document a hierarchical progression across the pathway from a spike-timing based code, where spikes are aligned to individual cycles of the sound envelope (often measured using vector strength), to an average rate-code which is more prevalent at and above the inferior colliculus. By using measures of discrimination and classification performance derived from neuronal responses, studies of sound envelope encoding have explicitly addressed hypotheses about how information in different parts of the auditory pathway could contribute to sound envelope perception (Downer et al., 2017, 2021; Henry et al., 2016; Johnson et al., 2012; Mackey et al., 2024a; Nelson and Carney, 2007; Sayles et al., 2013; Yao and Sanes, 2021), with two of the critical findings being that 1) small populations of neurons in the brainstem, midbrain, and cortex encode information sufficient to account for detection and discrimination of amplitude modulation depth and frequency (Downer et al., 2021; Johnson et al., 2012; Mackey et al., 2024a; Nelson and Carney, 2007; Penikis and Sanes, 2023; Sayles et al., 2013; Shi et al., 2024), and 2) there are notable differences in encoding schemes in primary vs. secondary auditory cortex (Downer et al., 2017; Johnson et al., 2024). The use of small populations (empirical or simulated) has been a key aspect of these studies. In regions such as A1, single-neuron measures have suggested temporal information not to be present in sufficient quantities to account for the perception of AM based

on, for instance, the population's average vector strength alone (Johnson et al., 2012). However, subsequent studies utilizing decoding methods, which are agnostic to the presence of a rate vs. temporal code, have revealed that temporal information is preserved in the population (Downer et al., 2021). These findings informed the present study's use of decoding methods on population-level activity measures.

In the study of AM encoding, the consideration of species is important for many reasons, and we focus on three here: 1) Primates (human and nonhuman) display greater perceptual sensitivity to AM than most animal models such as rodents and parakeets (Mackey et al., 2024a; Moody, 1994), 2) nonhuman primates (NHP) display more temporally precise AM encoding than rodents (Hoglen et al., 2018), and 3) primate auditory cortex exhibits a specific three-stage hierarchical anatomical organization, core-belt-parabelt, that provides the closest approximation of human auditory cortex available in animal models (Hackett et al., 2001, 2014). Previous studies of human auditory cortex report hierarchical progressions in speech encoding (Hamilton et al., 2021; Zion Golumbic et al., 2013) (e.g. Heschl's gyrus vs. Superior Temporal Gyrus) and interhemispheric differences in the encoding of sound envelope (Boemio et al., 2005). Namely, the left hemisphere preferentially encodes higher frequency envelope fluctuations, while the right hemisphere preferentially encodes lower frequency envelope fluctuations; and Heschl's gyrus encodes spectrotemporal speech features more precisely than the Superior Temporal Gyrus, which encodes higher level (e.g. semantic) information. The NHP model provides an opportunity to understand what circuits generate these transformations in encoding by characterizing AM encoding in different cortical circuits within area, and across the cortical hierarchy. For instance, it is possible that the hemispheric specialization reported previously is inherited from subcortical regions.

Laminar multielectrode studies (simultaneous recording across cortical layers) in auditory cortex have provided insight into the function of different intracortical and thalamocortical circuits in encoding temporal sound patterns involved in streaming (Banno et al., 2023; Fishman et al., 2001, 2004; Lakatos et al., 2013), intermodal audiovisual attention (Lakatos et al., 2009; Mehta et al., 2000b, 2000a; O'Connell et al., 2014, 2015), and pitch perception of click trains (Steinschneider et al., 1998). But there is a dearth of NHP studies of AM encoding in the superior temporal gyrus, containing the higher-order parabelt region of auditory cortex; moreover, there are no published studies of AM encoding as a function of physiologically

identified cortical layers in NHPs. Thus it is likely that studies of AM encoding with laminar resolution across the cortical hierarchy could yield insights into the thalamocortical and intracortical circuits utilized for AM encoding, and temporal sound pattern encoding more generally, in humans. To address this, here we report the encoding of AM signals as a function of cortical layer and hemisphere in the NHP primary and parabelt auditory cortex.

Materials and Methods

All experimental procedures were approved by the Institutional Animal Care and Use Committee of the Nathan Kline Institute (NKI).

Surgical procedures. Five nonhuman primates (Macaca mulatta, two female) C, H, Q, S, and W were implanted with headposts and recording chambers. Recordings from area A1 were done in chambers positioned to aim penetrations perpendicular to the supra temporal plane (Male W in the right hemisphere, female H in the left hemisphere, male S in the left hemisphere, Female C bilaterally). Three NHPs were also implanted with superior temporal gyrus chambers (female Q only on the left, female H only on the left, male W bilaterally). Surgical details for accessing primary and parabelt auditory cortex have been described in our previous publications (Kajikawa et al. 2017; Kajikawa et al. 2015). Specifically, based on presurgical MRI, the chambers were positioned to aim penetrations (during weekly acute recordings) perpendicular to the lower bank of the lateral sulcus, in the case of primary auditory cortex. For accessing the parabelt, presurgical MRI was used to target the superior temporal gyrus (STG) via multiple landmarks, which aided in positioning optimally over the STG: the superior temporal sulcus (~20 mm above the ear canal and ~10 mm above the zygomatic arch over AP 0-20 mm), the lateral sulcus, and the zygomatic arch (described extensively in Kajikawa et al. 2015).

Identification of recording locations

Utilizing the surgical approach described above, we were able to access the areas of the lateral sulcus and superior temporal gyrus that corresponded to area A1 in primary auditory cortex, and the parabelt region of the superior temporal gyrus. We approached primary auditory cortex perpendicular to the layers. Recording sites were functionally defined as belonging to A1, as opposed to R, RT, or Belt, based on the sharpness of tuning, tonotopic progression, sensitivity to

tones vs. noise, and granular layer onset latencies to BF tones (Lakatos et al., 2005; Merzenich and Brugge, 1973; Rauschecker, 1997).

We have previously published on the identification of the parabelt, its potential tonotopic organization, and other aspects of its topography in the same NHPs reported in the present dataset (Kajikawa et al., 2015; Mackey et al., 2024b). As described in these studies, and described in *Surgical Procedures,* a combination of pre-surgical MRI and laterally angled recording chambers permitted us to penetrate perpendicular to the cortical layers during acute weekly recordings.

Stimulus parameters. While NHPs sat awake, AM noise or click trains were presented with randomized modulation frequency (AM noise) or presentation rate (clicks). For brevity, the term modulation frequency will be used throughout the manuscript to describe the presentation rate of the click trains. Modulation frequencies utilized in this study were 1.6, 3.1, 6.3, 8.8, 12.5, 17.5, 25, 36, 50, 71, 100, and 200 Hz. Signals were 640 ms long, 70 dB PL, 100% modulated, and were ramped on/off using a linear ramp that was 5 ms in duration.

Electrophysiological signal processing. Data collection was conducted as described previously (Kajikawa et al., 2017; Mackey et al., 2024b). U-probes (Plexon) with a linear array of 23 channels (0.3– 0.5 MΩ at 1.0 kHz) at intervals of 100 or 200 micrometers between channels were used. Signals from all channels were amplified 10x, followed by 500x amplification before multiplexing and filtering. Each channel recorded field potentials (FP) (0.1–500 Hz) and MUA (500–5000 Hz using zero phase shift digital filtering, 48 dB/octave and rectified) simultaneously. When compared directly, the envelope MUA utilized here provides similar responses, and estimates of tuning, to thresholded multiunit spiking activity (Kayser, Petkov, Logothetis 2007; Super and Roelfsema, 2005; Shaheen and Liberman 2018), which supports the idea that our results are comparable to previous multiunit studies of click train and amplitude-modulation encoding. Moreover, a previous study found that AM encoding properties of single- and multi-unit clusters corresponded closely (Langner and Schreiner, 1988). Both envelope MUA and FP were sampled at 2 kHz and stored for offline analyses.

Data Analysis

Current source density (CSD) was calculated as the second spatial, i.e. across-channel, derivative of the FP for each time point of the laminar CSD profile (Freeman and Nicholson, 1975; Kajikawa and Schroeder, 2011; Mitzdorf, 1985).

Phase-locking value. The phase locking value of CSD and MUA signals at individual channels were computed at each modulation frequency (1.6-200 Hz) using complex demodulation, equivalent to a Discrete Fourier Transform coefficient at a given modulation frequency (Lu et al., 2022; Tallon-Baudry et al., 1996). For each trial k, a signal (duration T), windowed by Hann function $w(t) = \frac{1}{2}\left(1 - cos\left(\frac{2\pi t}{T}\right)\right)$, was convolved with a narrowband kernel, $f(t) = e^{-2\pi i f t}$ as $a_k = \frac{1}{T}\int_{t=0}^{T} x_k(t) \cdot w(t) \cdot f(t)\, dt$. The resultant coefficient, a_k, is a complex, and its argument, $\varphi_k = \arg(a_k)$, depends on the timing of MUA fluctuation relative to the cycle of the band. The phase-locking value was derived from all N trials as $PLV = \left|\frac{1}{N}\sum_k^N e^{i\varphi_k}\right|$. PLV is mathematically the same vector-length statistic used for vector strength of spike trains. In classical vector strength, the phases are taken at each spike time relative to the stimulus cycle. When computing PLV for continuous signals, the phase of the narrowband signal is calculated per trial by complex demodulation at the modulation frequency, yielding phases across trials. Both measures quantify the concentration of phase angles on the unit circle for each cycle of the stimulus from 0-1, with 1 being perfect synchrony, but PLV is better suited for our continuous CSD and MUA signals. And because we aggregate many cycles within each trial before taking the across-trial resultant, we avoid inflating sample size by counting cycles as independent; the degrees of freedom are the trials. This makes our PLV comparable to spike-based vector strength while remaining appropriate for continuous signals.

$$\text{[Equation 1]} \quad f(t) = e^{-2\pi i f t}$$

$$\text{[Equation 2]} \quad w(t) = \frac{1}{2}\left(1 - cos\left(\frac{2\pi t}{T}\right)\right)$$

$$\text{[Equation 3]} \quad a_k = \frac{1}{T}\int_{t=0}^{T} x_k(t) \cdot w(t) \cdot f(t)\, dt$$

$$\text{[Equation 4]} \quad PLV = \left|\frac{1}{N}\sum_k^N e^{i\varphi_k}\right|$$

To statistically evaluate phase-locking, we constructed a random-phase null distribution (n = 1,000 permutations) that preserved the trial's demodulated amplitude. We computed the observed amplitude-weighted vector, and estimated a *p-value* as the proportion of surrogates with a weighted vector greater than our observed weighted vector. We corrected for multiple comparisons across electrode channels using the Benjamini Hochberg method (Benjamini and Hochberg, 1995). For reference, we also computed corrected p-values from the more conventional Rayleigh's test, which provided qualitatively similar significance across the dataset. To compute mean PLV across the dataset, only channels estimated to be within a layer-compartment, with significant PLV were utilized.

Decoding Analysis and Mutual Information Estimation. To assess the decoding of stimulus identity from multichannel neural activity, we employed a multivariate classification and mutual information (MI) analysis pipeline based on linear discriminant analysis ("fitdiscr" in MATLAB; Statistics and Machine Learning Toolbox). This method fits a multivariate Gaussian model to each stimulus condition. The algorithm estimates the class-conditional means and a pooled covariance matrix, and constructs linear discriminant functions for each class. Each trial is then classified by assigning it to the class with the highest posterior probability, under the assumption of normally distributed features with equal covariance structure. This approach is equivalent to finding the linear projection that maximizes separation between class means while minimizing within-class variance. The analysis was conducted separately for each penetration site (i.e. recording session/experiment) and signal type (MUA or CSD) using custom-written MATLAB scripts. For each dataset, electrophysiological recordings were imported and epoched from -50 to 700 ms relative to stimulus onset and baseline corrected (-50 to 0 ms). Data used for decoding consisted of the time-domain signal from each trial and channel. For each layer (supragranular, granular, infragranular), only channels estimated to be within that cortical layer compartment were included for decoding. For each channel and decoding window, data were segmented into non-overlapping bins; unless otherwise specified, the decoding window was the entire baseline corrected 700 ms window after the stimulus onset, and we qualitatively inspected the pre-stimulus interval to ensure there was no difference in chance-level decoding; additionally, chance performance in the pre-stimulus interval is included in the figures. Linear discriminant

analysis (LDA) classifiers were trained using fourfold cross-validation to predict stimulus condition labels from trial-wise data. A confusion matrix was computed for each fold, and the resulting matrices were averaged across folds to yield a single empirical confusion matrix per electrode channel, time window, and permutation. This calculation was repeated 1000 times to compute the 95% confidence intervals (CI) around "True MI" depicted in the results section. To compute chance performance, decoding analyses were repeated 1000 times with trial labels randomly shuffled. For each permutation and each decoding window, mutual information was computed from the resulting confusion matrix using the following formulation:

$$MI = \Sigma \{i,j\} P(i,j) \cdot log_2 [P(i,j) / (P(i) \cdot P(j))]$$

where P(i,j) is the joint probability of predicted and true labels, and P(i), P(j) are the marginal probabilities. MI was computed for both true and shuffled label conditions for all decoding time-windows, channels, and permutations. The resulting distributions were used to compute mean MI and 95% confidence intervals under both empirical and null conditions.

Statistical analysis. In all cases, criterion for significance was 0.05, and results requiring correction for multiple comparisons (e.g. the phase-locking values) were corrected via the Benjamini-Hochberg correction (see section on phase locking value). Linear mixed-effects model (LME) analysis was conducted using "fitlme" in MATLAB. We report the t-statistic given by fitlme, which is similar to the F-statistic often reported for multifactorial models. The t-statistic quantifies the strength and direction of the effect as the ratio of the coefficient estimate and its standard error. For mutual information analyses, only channels where the Mutual Information lower CI exceeded the shuffled (chance) Mutual Information upper CI were retained for statistical analysis. To account for the nested structure of the data (multiple channels per recording), we modeled MI as a function of three fixed effects: cortical layer (supragranular, granular, infragranular), area (A1 vs. parabelt), and hemisphere (left vs. right), including their two-way interactions. Individual channels were included as a random intercept term. Significant effects of layer, area, and hemisphere indicate a significant difference from the reference groups, which were the supragranular layers, area A1, and the left hemisphere. For best modulation

frequency analysis, only channels where the bootstrapped lower CI exceeded the shuffled (chance) upper CI were retained for analysis.

In many nonhuman primate (NHP) neurophysiology experiments, including the present study, neural data are collected from many electrode contacts distributed across cortical layers and penetrations, across experimental sessions. In this context, the relevant statistical question is whether a given factor—such as cortical layer, area, or hemisphere—has a systematic effect on the measured neural variable (e.g., mutual information) across the population of recorded channels. This is distinct from testing whether different NHPs statistically differ from each other, which is a question that NHP studies are usually not adequately powered to address (Fries and Mars 2020). Accordingly, the degrees of freedom in our mixed-effects model reflect the number of auditory-responsive channels (with significant decoding accuracy) positioned in grey matter (confirmed using the CSD and MUA laminar response profile), recorded across sessions. For the CSD signal, we considered that the spatial resolution of the derived signal only permitted the isolation of a single sink (negativity), corresponding to a local synaptic current, in each layer compartment (supragranular, granular, infragranular). Thus we retained a single CSD channel per layer category for analysis, which corresponded to the largest sink (negativity) in that layer compartment, per recording. This limited our statistical power when analyzing CSD, and thus we mainly focus on multiunit activity when evaluating significance claims. For the multiunit activity signal, all auditory-responsive channels, with significant decoding accuracy, were retained for analysis, often totaling approximately 700-1000 channels across the dataset. Treating individual channels' MUA as measuring different local populations is supported by our electrode spacing (100-200 micrometers), and the observation that neighboring channels displayed markedly different response characteristics (e.g. latency) and decoding accuracy.

Results

Field potential and multiunit spiking activity were measured using linear array "laminar" multielectrode probes (see Methods) in response to amplitude-modulated noise, and click trains of different frequencies (i.e. repetition rates) in area A1 (AM noise, n = 42; Clicks, n = 63) and parabelt auditory cortex (AM noise, n = 88; Clicks, n = 84) across four rhesus macaques (*Macaca mulatta*); here, n refers to cortical sites, i.e. penetrations/experiments with the multielectrode probe. In all recordings, the electrode was angled to be perpendicular to the

276 cortical layers, and then straddled the layers during the recording (see Methods). From the field
277 potential, current source density was calculated as the second derivative across electrode
278 channels to mitigate volume conduction, and to estimate local transmembrane currents in
279 specific cortical layer compartments with specific spatial resolution given by the interelectrode
280 distance (100-200 micrometers). Using the frequently encountered activation pattern,
281 characterized by an early onset, sharp L4 sink (negative CSD) co-localized with multiunit
282 activity, followed by L2/3 and L5/6 CSD activation, individual electrode channels were assigned
283 to the supragranular (L2/3), granular (L4), and infragranular (L5/6) compartments (Kajikawa et
284 al., 2015; Lakatos et al., 2005b; Steinschneider et al., 1992). Using this layer-identification
285 procedure, we separated our data into local neuronal populations in the supragranular, granular,
286 and infragranular layers for further analysis. This allowed us to utilize multiple channels of data
287 per experiment, and to evaluate hypotheses about the function of neuronal populations in
288 different cortical layer compartments. Figure 1 shows trial-averaged CSD and MUA responses to
289 AM noise of different modulation frequencies. Figure 1A depicts the response to 3.1 Hz AM
290 noise in a representative area A1 site, exhibiting an early (~15 ms), sharp CSD sink (negativity,
291 red in the color map) characteristic of the thalamorecipient granular layer. The multiunit activity
292 derived from the same signal exhibits an early peak around in the same electrodes. The
293 supragranular and infragranular CSD signals exhibited longer latencies, as expected, which
294 resulted in relatively steady-state (as opposed to phase-locked) responses to the higher
295 modulation frequency signals (Figure 1B-D). Figure 1E depicts an example parabelt site, where
296 laminar response profiles displayed more diversity than area A1, which we have previously
297 described (Kajikawa et al., 2015; Mackey et al., 2024b). A notable difference between the site in
298 Figure 1G-H and Figure 1C-D is that the parabelt multiunit activity displays less phase-locking,
299 though there is noticeable rhythmicity to the late MUA suppression that could contribute to
300 discrimination between modulation frequencies (Figure 1G). Summary phase-locking values (see
301 Methods) are depicted in Figure 1I-L. Across layers, similar phase-locking was observed, on
302 average, in both the CSD and MUA signal. The phase-locking was consistent with previous
303 reports using CSD and MUA in A1. The parabelt differed noticeably from area A1 in that
304 significant phase-locking was almost never observed above 10 Hz. We restricted calculation of
305 the mean to frequencies at which more than 10 local neuronal populations (i.e. channels)
306 displayed significant PLV (Figure 1I-L). The highest frequency at which significant phase-

locking was observed was similar across layers, but differed between areas. In area A1 ($n = 42$ sites), the mean (across sites) maximum values were as follows for current source density: 164.8 Hz (SD: 68.1) for the supragranular layers, 172.5 (SD: 59.8) for the granular layer, and 161.6 (SD: 70.3) for the infragranular layer compartment. In area A1, multiunit activity provided similar estimates of maximum frequency of PLV: 152.7 Hz (SD: 69.9) for the supragranular layers, 169.1 Hz (SD: 66.2) for the granular layer, and 170.3 (SD: 68.4) for the infragranuar layer compartment. In the parabelt ($n = 88$), the maximum frequency at which significant phase-locking could be observed was noticeably lower; the values for the current source density signal were as follows: 50.5 Hz (SD: 54) for the supragranular layers, 42.2 (SD: 56.1) for the granular layer, 50.3 Hz (SD: 54.9) for the infragranular layers. For the multi-unit activity in the parabelt, the values were 35.5 Hz (SD: 64.9) for the supragranular layers, 22.9 Hz (SD: 38.5) for the granular layer, and 26.9 Hz (SD: 36.9) for the infragranular layers. In A1, the differences between the layers in maximum frequency phase-locking were significant for the MUA signal after Benjamini-Hochberg correction ($\chi^2(2) = 10.4$, $p = 0.006$), but not significant for the CSD signal ($\chi^2(2) = 2.6$, $p = 0.26$). In the parabelt, the differences between the layers in maximum frequency phase-locking were significant for the CSD signal after Benjamini-Hochberg correction ($\chi^2(2) = 11.4$, $p = 0.003$), but not significant for the MUA signal ($\chi^2(2) = 1.1$, $p = 0.59$). The effect of brain area was significant after Benjamini-Hochberg correction for all layer categories for the CSD and MUA signals (Friedman's test; $\chi^2(1) > 9.0$, $p < 0.01$). While neuronal responses can be summarized using average amplitude or phase-locking measures, the underlying waveform is complex, particularly for continuous signals such as the CSD and envelope MUA depicted here. This motivated our use of decoding methods to assess information present in the response waveforms across our dataset.

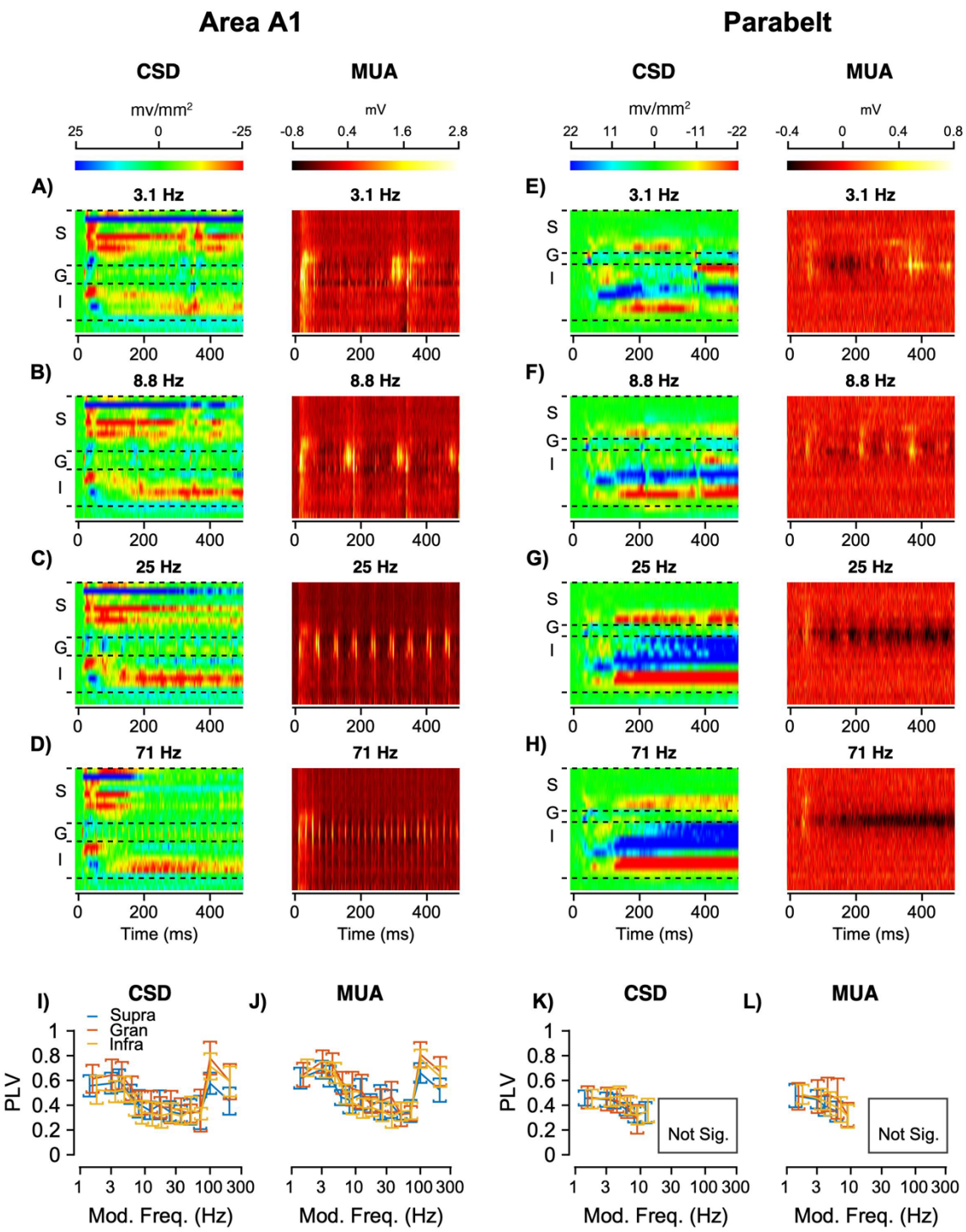

Figure 1 – Representative laminar activity profiles in response to sinusoidally amplitude modulated noise of different frequencies, and phase-locking values across the data set. The

333 left column (**A-D**) show trial-averaged responses (*n* = 50 trials) from a representative recording
334 site in A1 to sinusoidally amplitude modulated (AM) noise of different frequencies. The right
335 column shows trial-averaged responses (*n* = 50 trials) from a representative site in the parabelt
336 (**E-H**) to SAM of different modulation frequencies. These sites, and all of our recordings, were
337 approached such that the electrode contacts were perpendicular to the cortical layers. A phase-
338 locking value was computed for all recordings, which are displayed for each layer and signal
339 type (CSD and MUA) for area A1 (**I** and **J**; mean and 95% CIs; *n* = 42 penetrations/sites) and the
340 parabelt (**K** and **L**; mean and 95% CIs; *n* = 88 penetrations/sites). PLV was slightly jittered along
341 the x-axis to enable visibility of the different data traces; in all cases, the modulation frequencies
342 were the same (see Methods).
343
344 *Classifying modulation frequency based on current source density and multiunit activity*
345 To quantify how CSD and MUA encode information about AM stimuli, we utilized linear
346 discriminant analysis (LDA; see Methods), and calculated Mutual Information (MI). MI is useful
347 because it quantifies decoding accuracy across conditions, and the systematicity of decoding
348 errors, as opposed to averaging accuracy across conditions. Figure 2 depicts the representative
349 core and parabelt sites from Figure 1, with the LDA-derived confusion matrix for a channel in
350 the granular layer for both sites (Figure 2A; Figure 2E), with MI values (right-hand panel) for all
351 channels across layers (the y-axis). The color maps and MI plots were scaled the same across
352 conditions and to emphasize the differences between area A1 and parabelt. Noticeably, area A1
353 exhibited nearly perfect decoding accuracy across conditions (Modulation frequencies). For
354 example, the color map in Figure 2A indicates that most conditions were predicted correctly
355 based on the granular channel CSD response in 100% of trials; and the granular channel MUA
356 decoding was similar (Figure 2B). Across channels, it can be seen that MI, which provides an
357 information theoretic metric for stimulus information across different stimulus conditions (i.e.
358 across the entire confusion matrix). 12 modulation frequencies were utilized, yielding a
359 maximum possible MI value of about 3.5 bits ($\log_2(12) = 3.5$), which further emphasizes how
360 accurate the site in Figure 2A-D is. Interestingly, though the overall decoding accuracy was
361 similar, the laminar profile of MI differed between AM noise and clicks: supragranular MUA,
362 for example, exhibited MI values not significantly different than the infragranular channels in

response to clicks, while AM noise did not elicit such a strong response in the supragranular MUA.

Relative to area A1, the parabelt demonstrated reduced decoding accuracy and MI, likely due to the parabelt's higher position in the processing hierarchy (Figure 2E-H). Though the granular channels exhibited the highest MI for this example, in the next figure we will show that the MI distributions were broader, i.e. there was more variability in the parabelt dataset than in area A1; thus, though the extragranular layers encoded very little information in this example, across the dataset they often displayed significant, above chance MI.

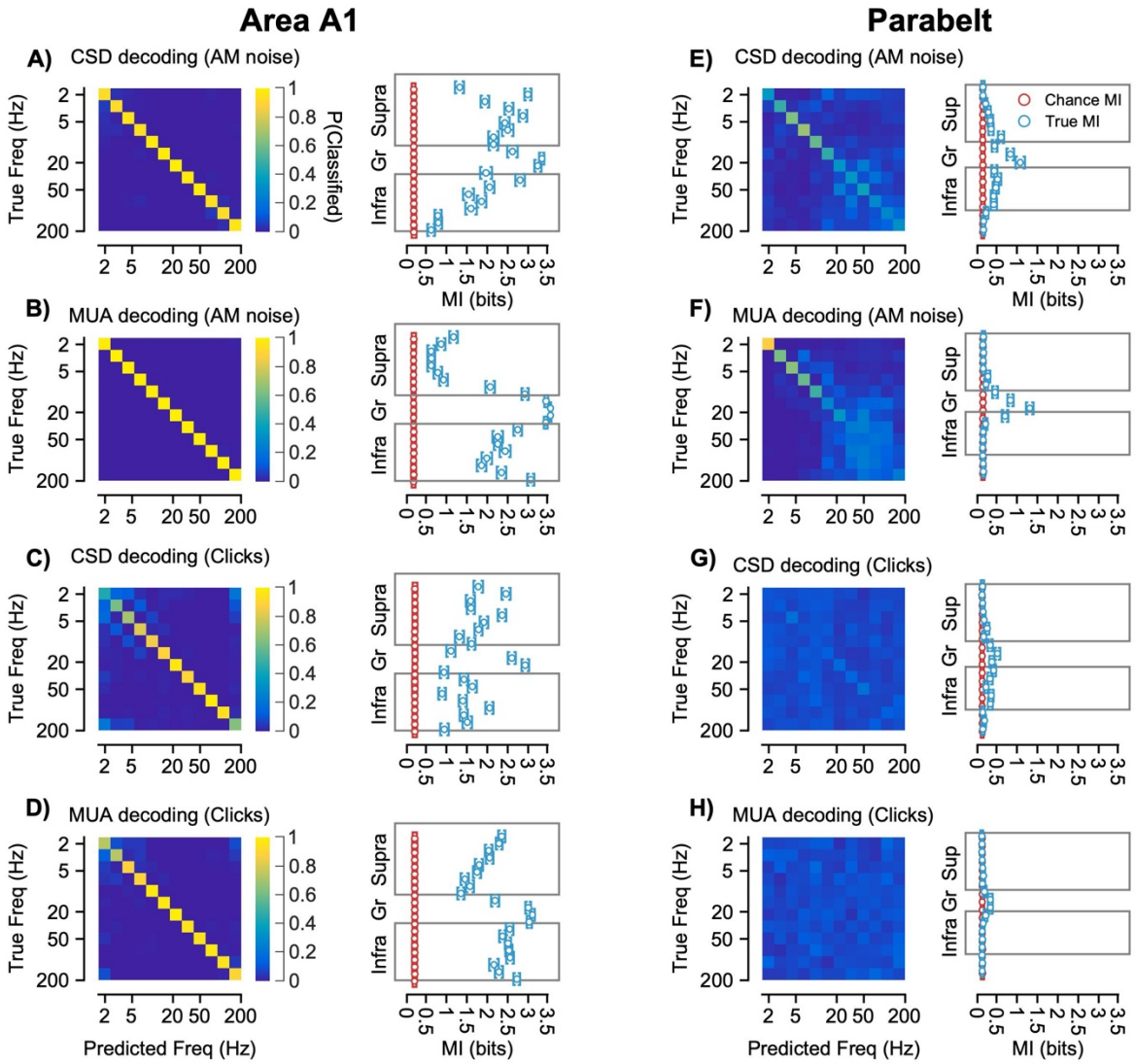

Figure 2 – Representative example decoding results from AM noise and click-train evoked responses from the recording sites in Figure 1. The left panels depict the confusion matrices which quantify the decoding accuracy (0-1) in each condition for a channel in the granular layer.

The predicted condition is indicated on the x-axis, and the true condition indicated on the y-axis. The color axis represents the proportion of classifications across 50 trials. The mutual information (MI) values for all channels are plotted on the x-axis of each panel on the right. Observed, or "true" MI was computed as described in the Methods, and Chance MI was calculated after shuffling the condition labels. For the example in area A1, the confusion matrices for a channel in the granular layer (layer 4) are shown in response to AM noise (**A** and **B**), and click trains (**C** and **D**), with corresponding mutual information values of all channels, which were calculated on the confusion matrices. Panels **E-H** depict the same analysis for the example in the parabelt.

In the MI plots, channels are labeled as being in the supragranular (Supra), granular (Gr), or infragranular (Infra) layer compartments. Color maps are scaled 0-1, and mutual information plots are scaled 0-3.5 bits (the maximum possible MI with 12 stimulus conditions). Error bars represent 95% confidence intervals calculated across 1,000 permutations.

Interhemispheric, interareal, and interlaminar differences in AM noise encoding

Across the dataset, we observed differences in AM encoding in different hemispheres, areas, and cortical layers. Figure 3 displays cumulative distributions of the MI values derived from CSD and MUA signals in the different hemispheres, layers, and cortical areas. Throughout the analyses presented here, the CSD and MUA will be shown, but statistical testing was reserved for the MUA results for statistical reasons (see Methods).

A mixed effects model was used to quantify the effects of each factor, and accounted for between-channel, and thus between-NHP variability (see Methods). MI was used as the dependent variable, while layer, area, and hemisphere were used as the independent variables (see Methods). Mixed-effects modeling revealed that mutual information (MI) was modulated by significant two-way interactions, which qualified the interpretation of main effects (Table 1). The reference groups for area, layer, and hemisphere were area A1, the supragranular layers, and the left hemisphere, respectively; i.e. all effects are quantified relative to these reference groups.

The first novel finding was that the hierarchical differences between area A1 and parabelt differed across layers. The main effect of area was that was reduced MI in the parabelt, though this differed across layers (Table 2). Specifically, enhancement of MI in the granular and infragranular MUA across the dataset (Rightward shift in the orange and gold traces in Figure 3

E-F; Table 1), was attenuated in the parabelt relative to area A1, quantified by a significant negative interaction of granular layers with parabelt, and infragranular layers with parabelt in the AM noise and click datasets (Table 1 and 2). These results indicate that hierarchical transformations in encoding are not uniform across the auditory pathway, but differ in specific thalamocortical (granular A1) and intracortical (extragranular A1 and parabelt) circuits, which will be considered in more depth in the Discussion section.

Consistent with previous work in human and nonhuman primate auditory cortex (Boemio et al., 2005; O'Connell et al., 2015) (also see Discussion section), the right hemisphere displayed reduced mutual information about AM relative to the left hemisphere (Tables 1-2). The positive statistical interaction, *Layer*Hemisphere*, provides insight into how these hemispheric differences emerge: the granular and infragranular layer signals did not display left hemisphere dominance (Figure 3 A-B; Figure 3 C-D; Tables 1-2); and, in fact, the right hemisphere often displayed enhanced encoding, only in the deep layers, compared to the left hemisphere. When coupled with the main negative effect of the right hemisphere (Table 1), this indicates that the enhanced encoding in the left hemisphere is localized mainly to the supragranular layers, and is not inherited from the medial geniculate body (as would be expected if the granular layer displayed left-hemisphere dominance); moreover, the difference is visible in the distributions of supragranular MI, which is visibly shifted to the left in area A1 in Figure 3E (supragranular median 1.1 bits) vs. Figure 3F (supragranular median 0.8 bits). Similar strength of the granular and infragraular interactions with the right hemisphere were observed for the MI values calculated based on click train responses (Table 2). Together, these results highlight the importance of cortical layers when considering interhemispheric effects, and may aid in determining the circuit origin of hemispheric asymmetries, which will be further elaborated upon in the Discussion section.

A notable difference in the AM noise and click train conditions was that, in the infragranular right hemisphere parabelt dataset, less than twenty channels exhibited above-chance mutual information values. While this reinforces the finding that the left hemisphere and area A1 exhibit enhanced AM encoding, it suggests that click trains were not optimal for interareal comparisons. For this reason, the remaining analyses focus on the responses to AM noise.

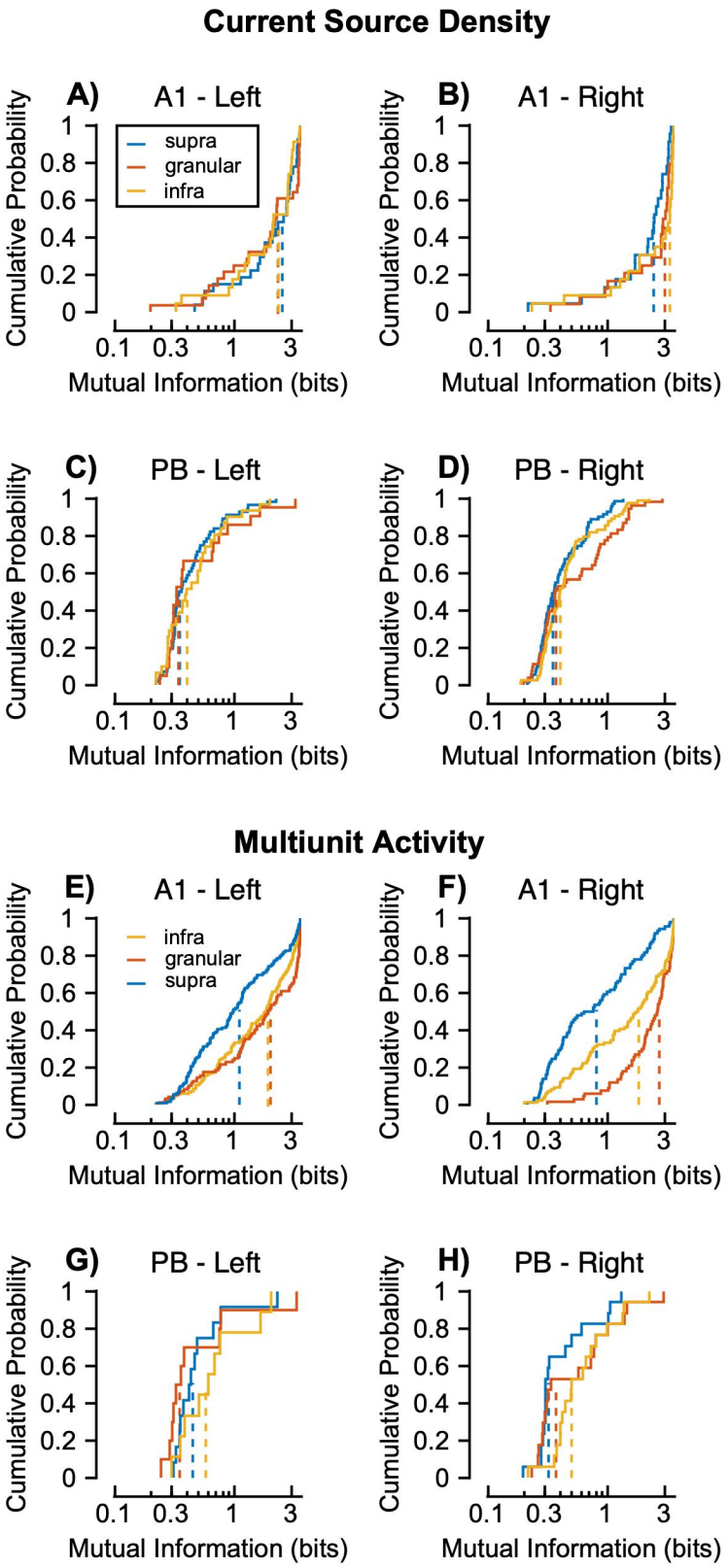
Current Source Density
A)
A1 - Left
supra
granular
infra
B)
A1 - Right
C)
PB - Left
D)
PB - Right
Multiunit Activity
E)
A1 - Left
infra
granular
supra
F)
A1 - Right
G)
PB - Left
H)
PB - Right
Cumulative Probability
Mutual Information (bits)
0
0.2
0.4
0.6
0.8
1
0.1
0.3
1
3

Figure 3 – Cumulative distributions of mutual information values extracted from responses to AM noise across areas, layers, and hemispheres. Distributions of MI values derived from the CSD signal are depicted for left (*n* = 27, 28, 23 supragranular, granular, and infragranular channels, respectively) and right (*n* = 23, 24, 23 supragranular, granular, and infragranular channels, respectively) hemispheres of area A1 (**A-B**), and the left (*n* = 12, 10, 9 supragranular, granular, and infragranular channels, respectively) and right (*n* = 17, 20, 17 supragranular, granular, and infragranular channels, respectively) hemispheres of the parabelt (**C-D**). Distributions of MI values derived from the MUA signal are depicted for left (*n* = 131, 97, 154 supragranular, granular, and infragranular channels, respectively) and right (*n* = 86, 67, 99 supragranular, granular, and infragranular channels, respectively) hemispheres of area A1 (**E-F**), and the left (*n* = 21, 24, 25 supragranular, granular, and infragranular channels, respectively) and right (*n* = 21, 39, 38 supragranular, granular, and infragranular channels, respectively) hemispheres of the parabelt (**G-H**). Only above-chance values are displayed (see Methods). Dashed lines demarcate the median value of each distribution.

Table 1 – Terms in a mixed effects model analysis of mutual information values extracted from MUA responses to AM noise (1.6-200 Hz). The reference groups were A1, the supragranular layers, and the left hemisphere. *Degrees of freedom* = 779.

Model: MI ~ Area + Layer + Hemisphere + Area*Layer + Layer*Hemisphere + Hemisphere*Area + (1|Channel)		
Term:	t-statistic	P-value
Right hemi (vs. L)	-2.2	0.025
Granular layer (vs. Supra)	5.4	$3*10^{-7}$
Infragranular layer (vs. Supra)	3.8	0.0001
Granular layer*Right Hemi	3.2	0.001
Infragranular*Right Hemi	1.8	0.06

Granular layer*Parabelt	-4.9	$8*10^{-7}$
Infragranular layer*Parabelt	-2.2	0.02
Right Hemi*Parabelt	-2.4	0.01
Parabelt	-1.8	0.86

Table 2 – Terms in a mixed effects model analysis of mutual information values extracted from MUA responses to click trains (1.6-200 Hz). The reference groups were A1, the supragranular layers, and the left hemisphere. *Degrees of freedom* = 997.

Model: MI ~ Area + Layer + Hemisphere + Area*Layer + Layer*Hemisphere + Hemisphere*Area + (1|Channel)		
Term:	t-statistic	P-value
Granular layer (vs. Supra)	5.5	$3.7*10^{-8}$
Infragranular layer (vs. Supra)	5.1	$5*10^{-7}$
Parabelt (vs. A1)	-6.8	$1*10^{-11}$
Infragranular layer*Right Hemisphere	4.0	$6*10^{-5}$
Granular layer*Right Hemisphere	3.45	0.0058
Granular layer*Parabelt	-2.7	0.0069
Infragranular*Parabelt	-2.4	0.0170
Right hemi*Parabelt	-2.7	0.0067
Right hemi (vs. L)	0.35	0.7

Topography of AM encoding in the parabelt

We next considered the hypothesis that caudal parabelt (CPB) exhibits enhanced AM encoding relative to rostral parabelt (RPB), based on CPB and RPB's putative positions in the dorsal and ventral streams (Camalier et al., 2012; Hackett et al., 1998; Romanski et al., 1999). We quantified how mutual information about AM varied across the two-dimensional map of each NHP's parabelt area using linear regression, which took the form "*Mutual Information ~ X coordinate + Y coordinate*." Mutual information did not significantly vary as a function of X ($t = 0.6$, $p = 0.5$) or Y coordinate ($t = -1.8$, $p = 0.07$). Moreover, neither X nor Y position significantly correlated with mutual information value (Spearman's $R < 0.2$; $p > 0.05$). This can be seen in the representative example maps in Figure 4, which indicate that AM encoding did not systematically differ across the parabelt region in our dataset.

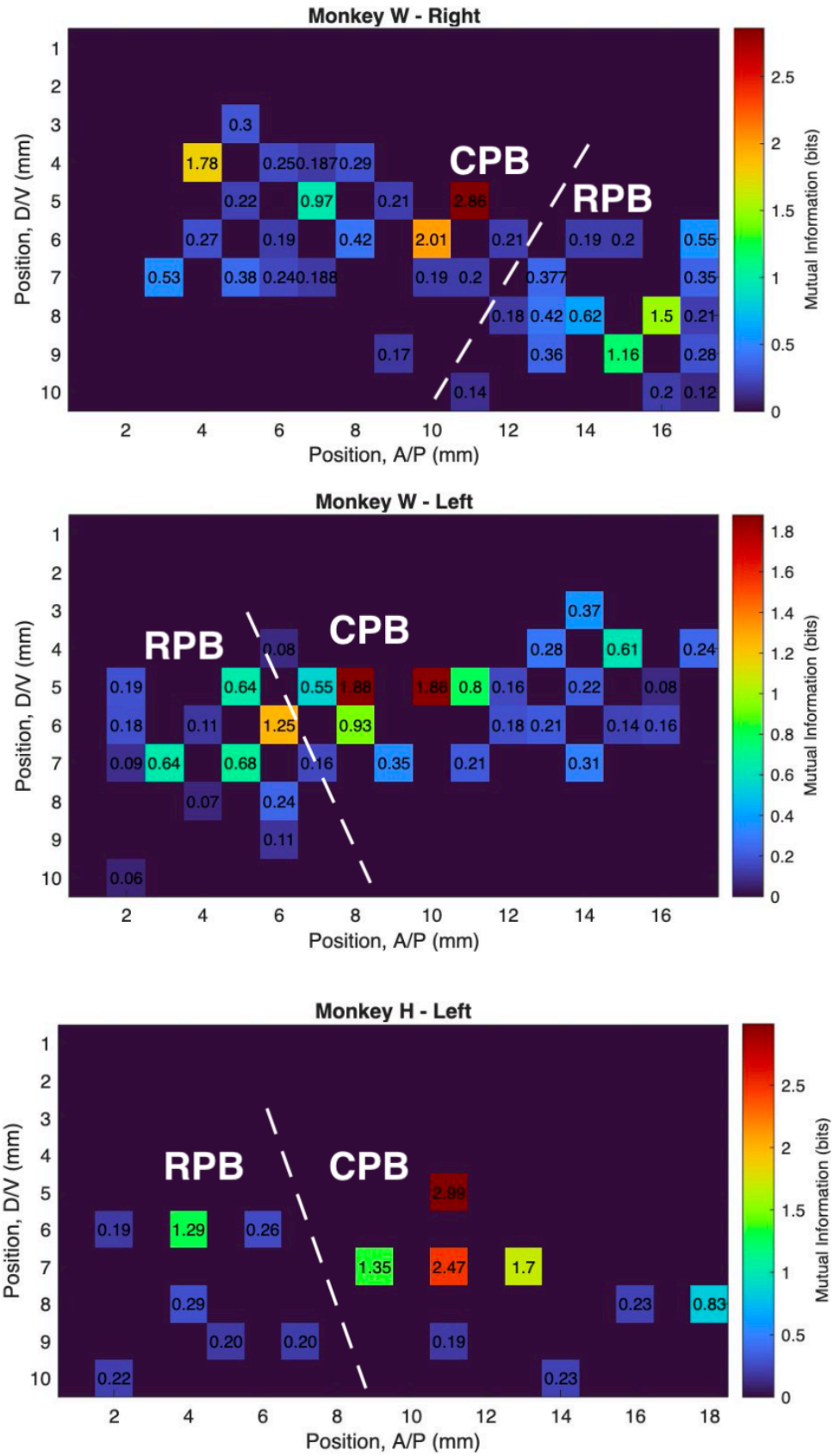
Monkey W - Right
CPB
RPB
Position, D/V (mm)
Position, A/P (mm)
Mutual Information (bits)
Monkey W - Left
RPB
CPB
Position, D/V (mm)
Position, A/P (mm)
Mutual Information (bits)
Monkey H - Left
RPB
CPB
Position, D/V (mm)
Position, A/P (mm)
Mutual Information (bits)

474

Figure 4 – Topographic analysis of AM encoding in parabelt auditory cortex. Color maps depict mutual information values derived from MUA responses to amplitude-modulation, as a function of the two-dimensional maps across parabelt auditory cortex in three representative cases. As a result of the parabelt recording chamber placement over the superior temporal gyrus, the X and Y coordinates are arbitrary positions in a two dimensional grid with 1 mm resolution. The X coordinates refer to anterior-posterior (A/P) dimension, and the Y coordinates refer to the dorsal-ventral (D/V) dimension. The border between the rostral parabelt (RPB) and caudal parabelt (CPB) was determined using tonotopic progression.

Preferred modulation frequency

Having characterized how mutual information differs across intracortical circuits in A1 and PB, we next sought to understand how their preferred modulation frequency differed. Among MUA channels that significantly encoded at least one modulation frequency, we observed that the parabelt encoded lower modulation frequencies than A1 in a mixed effects model (*Best MF ~ Hemisphere + Area + Layer (1|Channel);* Effect of Parabelt, $t = -4.4$, $df = 1536$, $p = 9*10^{-6}$). Best modulation frequency appeared to be higher in the infragranular layers of area A1 (Figure 5A), but this trend was not present in the parabelt dataset (Table 3; Interaction of Infragranular layers with Parabelt). Regarding hemispheric differences, the right hemisphere trended towards encoding lower modulation frequencies, and there was a significant positive interaction of right hemisphere with infragranular layers, which indicates that the infragranular layers encoded higher modulation frequencies than would be expected based on the right hemisphere main effect (Table 3).

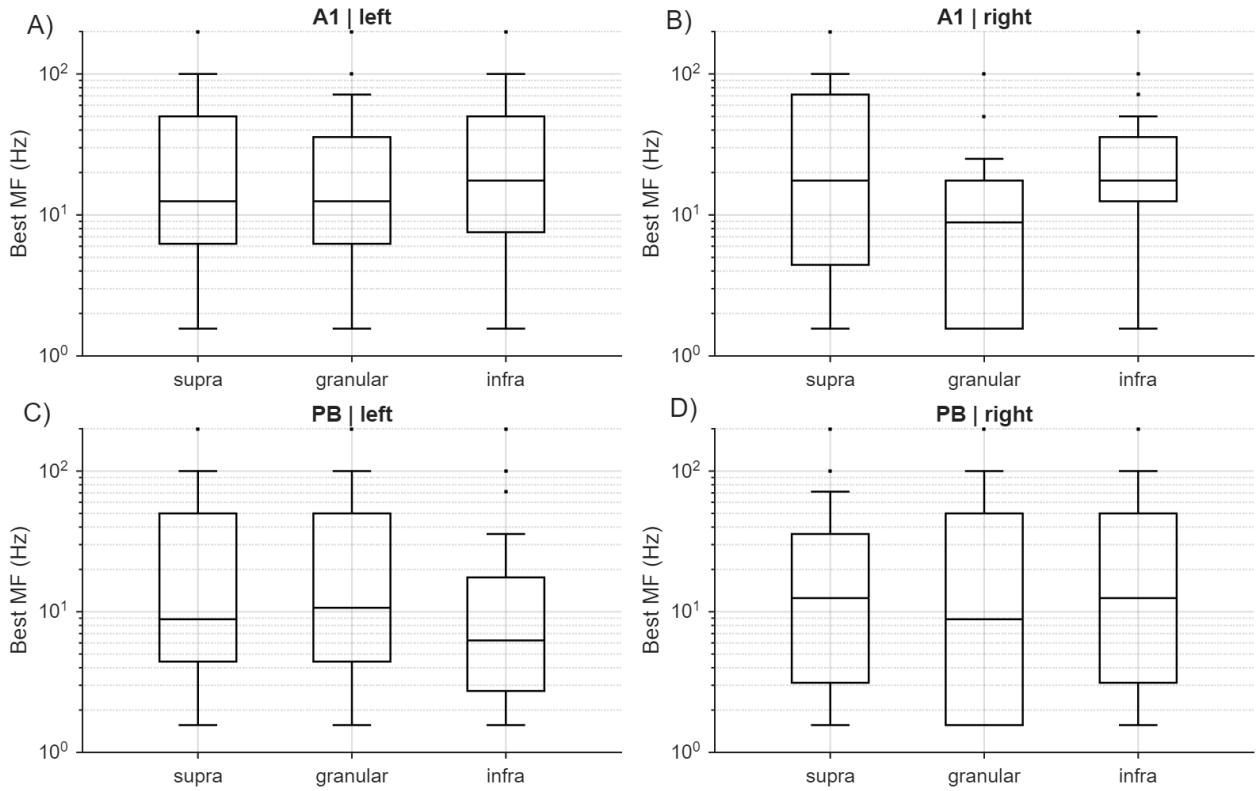

Figure 5 – Best decoded modulation frequency in area A1 and the Parabelt. A) Box-plots display the noise modulation frequency that elicited the highest decoding accuracy for multiunit activity in the left hemisphere, Area A1, in different cortical layers (Supragranular, n = 171 channels; Granular, n = 86 channels; Infragranular, n = 156 channels). B) Best decoded modulation frequency in the right hemisphere, Area A1 (Supragranular, n = 134 channels; Granular, n = 47 channels; Infragranular, n = 74 channels). C) Best decoded modulation frequency in left hemisphere Parabelt (Supragranular, n = 114; Granular, n = 46; Infragranular, n = 81). D) Best decoded modulation frequency in the right hemisphere Parabelt (Supragranular, n = 268; Granular, n = 124; Infragranular, n = 240).

Table 3 – Mixed effects model of best decoded modulation frequency. *Degrees of freedom* = 1534.

Model: Best MF ~ Area + Layer + Hemisphere + Area*Layer + Layer*Hemisphere + Hemisphere*Area + (1|Channel), Degrees of freedom = 1532.		
Term:	t-statistic	P-value
Right hemi (vs. L)	-1.2	0.21
Parabelt (vs. A1)	-1.6	0.09
Granular (vs. Supra)	-1.8	0.06
Infra (vs. Supra)	0.5	0.6
Infra*Right Hemi	2.9	0.004
Infra*Parabelt	-3.2	0.001

AM encoding over time

Having characterized how the encoding of AM differs across regions using the entire response waveform, it was then of interest to investigate how encoding unfolds across time, which can address questions, albeit indirectly, about spike-timing vs. spike rate codes in previous studies. Analyzing decoding results over time also addresses what time-points in the stimulus response may be driving the decoding accuracy in our previous results, which utilized the entire response waveform (e.g. Figures 1-3). To address these issues, responses were binned into 10 or 50 ms bins and the decoding process was repeated for each bin (see Methods). Figure 6 shows example decoding results over time, for the 6.3 Hz AM noise stimulus for core (Figure 6A-B) and parabelt (Figure 6C-D). These results complement the mutual information analyses, by showing that at a low modulation frequency (below ~25 Hz), sites in the parabelt often displayed far above-chance decoding accuracy. They also suggest that the highest magnitude response, in CSD or MUA, often encountered at the onset of the stimulus (Figure 1), does not always correspond to the peak decoding accuracy, which could be found throughout the duration of the stimulus response; i.e. maximum decoding occurred sparsely over time. Consistent with this, decoding accuracy of different modulation frequencies exhibited peaks throughout the response, from onset latency through 700 ms (Figure 7E-H) for both the CSD and MUA signals. These results also suggest that the time-varying aspect of the response to AM contributes heavily to its discriminability in both A1 and the parabelt (see Discussion). This observation likely depends on

our use of population-level activity, which has been found to exhibit robust temporal encoding in a previous single-unit study (see Introduction and Discussion; Downer et al. 2021).

To quantify these observations, the peak decoding time, across all modulation frequencies, was compared across layer, area, and hemisphere. The right hemisphere had significantly earlier peak times (Table 5), though this appeared to be restricted to area A1, indicated by the significant interaction of parabelt with the right hemisphere (Figure 7; Table 5). The parabelt had significantly later peak times in both the CSD and MUA signals. In the infragranular layers of the parabelt, MUA peak decoding times were earlier than predicted by the infragranular layer term on its own (Table 5). The same mixed effects model analysis revealed similar size and direction of effects for the 50 ms binned decoding results (Tables 6).

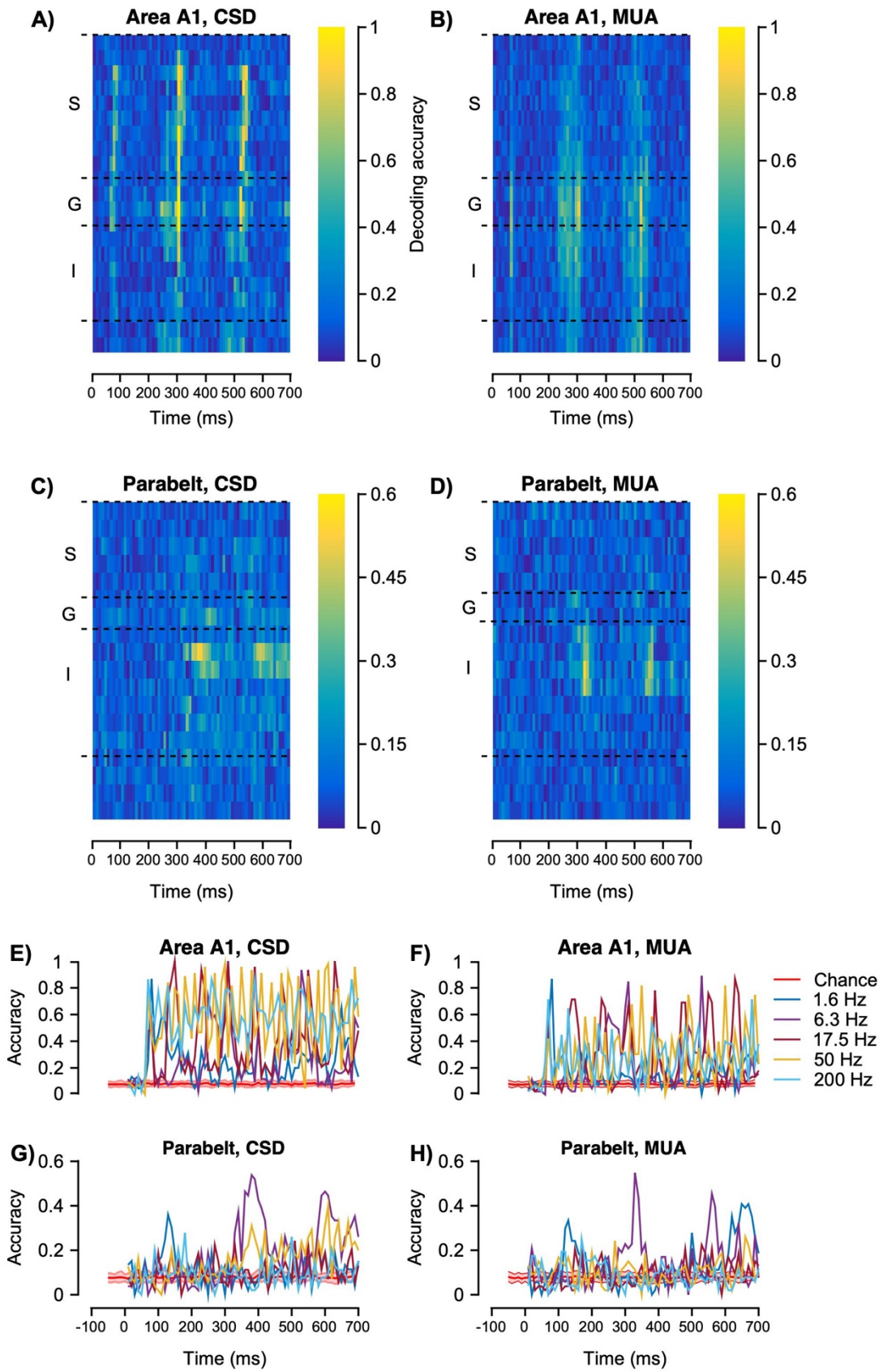
A)
Area A1, CSD
B)
Area A1, MUA
S
G
I
Decoding accuracy
0 100 200 300 400 500 600 700
Time (ms)
C)
Parabelt, CSD
D)
Parabelt, MUA
E)
Area A1, CSD
F)
Area A1, MUA
Accuracy
Chance
1.6 Hz
6.3 Hz
17.5 Hz
50 Hz
200 Hz
G)
Parabelt, CSD
H)
Parabelt, MUA
-100 0 100 200 300 400 500 600 700

549

Figure 6 – Decoding AM noise over time. A) Representative example of decoding the CSD signal over time, for the 6.3 Hz AM noise condition in left hemisphere area A1 (n = 50 trials). The decoding results for the same site's MUA are shown in (**B**). **C**) Representative example of decoding the CSD signal over time, for the 6.3 Hz AM noise condition in the right hemisphere parabelt auditory cortex (n = 50 trials). The decoding results for the same site's MUA are shown in (**D**). In all heat maps, the bin size was 10 ms. **E**) Decoding accuracy using the CSD signal from a granular layer channel (11) in panel (A) across a subset of modulation frequencies used in the study. **F**) Decoding accuracy using the MUA signal from A1 granular layer channel (11) in panel B across a subset of modulation frequencies used in the study. **G**) Decoding accuracy using the CSD signal from an infragranular layer channel (9) in panel (**C**) across a subset of modulation frequencies used in the study (1.6-200 Hz). **H**) Decoding accuracy using the MUA signal from an infragranular layer channel (11) in panel B across a subset of modulation frequencies used in the study. Chance level decoding was calculated after shuffling the decoding labels and is indicated by the red trace. Error bands represent 95% confidence intervals (1,000 permutations).

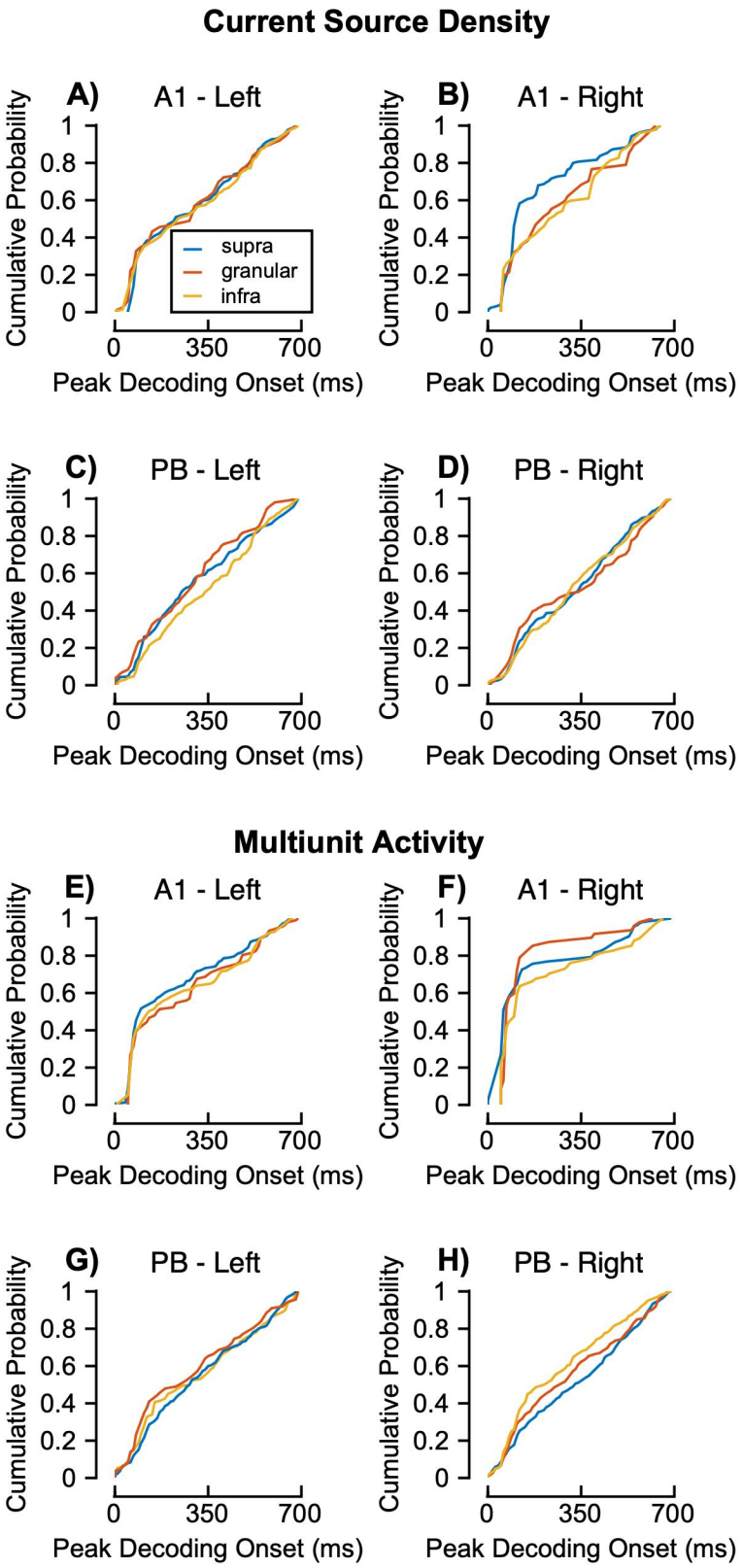
Current Source Density
A)
A1 - Left
B)
A1 - Right
C)
PB - Left
D)
PB - Right
supra
granular
infra
Cumulative Probability
Peak Decoding Onset (ms)
0
350
700
0
0.2
0.4
0.6
0.8
1
Multiunit Activity
E)
A1 - Left
F)
A1 - Right
G)
PB - Left
H)
PB - Right

Figure 7 – Cumulative distributions of peak decoding onset in core and parabelt in response to amplitude modulated noise using a 10 ms bin size. Distributions of peak decoding accuracy values, derived from the CSD signal, are depicted for left and right hemispheres of area A1 (**A-B**), and the parabelt (**C-D**). Distributions of peak values derived from the MUA signal are depicted for left and right hemispheres of area A1 (**E-F**), and the parabelt (**G-H**). Only above-chance values are displayed (see Methods).

Table 5 – Mixed effects model of peak decoding onset time in the MUA signal, using a 10 ms bin (significant terms only). *Degrees of freedom* = 1716.

Model: Peak Time ~ Area + Layer + Hemisphere + Area*Layer + Layer*Hemisphere + Hemisphere*Area + (1|Channel)		
Term:	t-statistic	P-value
Right hemi (vs. L)	-2.3	0.019
Parabelt (vs. A1)	5.1	$2*10^{-7}$
Infragranular (vs. Supra)	2.2	0.03
Infragranular layer*Parabelt	-2.8	0.0057
Right Hemi*Parabelt	2.9	0.004
Granular layer (vs. Supra)	0.7	0.4

Table 6 – Mixed effects model of peak decoding onset time in the MUA signal, using a 50 ms bin (significant terms only) *Degrees of freedom* = 1716.

Model: Peak Time ~ Area + Layer + Hemisphere + Area*Layer + Layer*Hemisphere + Hemisphere*Area + (1|Channel)		
Term:	t-statistic	P-value

Parabelt (vs. A1)	4.7	$3*10^{-6}$
Granular (vs. Supra)	2.1	0.03
Infragranular (vs. Supra)	2.4	0.01
Granular layer*Parabelt	-3.2	0.002
Infragranular layer*Parabelt	-2.6	0.007
Right Hemi (vs. L)	-1.3	0.2

Discussion

The present report builds on previous work on how sounds are encoded across the auditory cortical hierarchy. Rather than a uniform degradation of temporal precision, we found that deep-layer circuits in both A1 and parabelt maintain robust discriminability of amplitude-modulated sounds, suggesting that corticocortical and corticofugal pathways arising from these layers continue to carry temporally structured information; and the deep-layer enhancement in A1 was significantly reduced in the parabelt. Our results also indicate left-hemisphere enhancement in the supragranular layers, suggesting that hemispheric asymmetries in temporal processing may originate in the supragranular circuits specialized for interareal communication, as opposed to being inherited from thalamocortical projections.

Previous NHP studies have described hierarchical progressions in stimulus selectivity that coincide with the hierarchical increase in response latency in primary, secondary, and tertiary (parabelt) auditory cortex (Camalier et al., 2012). For instance, NHP studies of AM encoding have discovered notable differences in encoding between primary and secondary auditory cortex. Namely, while primary AC encodes AM depth with an increasing rate code, secondary belt auditory cortex exhibits an opponent (increasing/decreasing) code for AM (Downer et al., 2017; Johnson et al., 2024). Consistent with this, fMRI studies have noted some degree of selectivity for longer temporal intervals in nonprimary auditory cortices, particularly in

601 the parabelt (Dheerendra et al., 2021). An extended temporal integration window, and broad
602 frequency tuning likely contributes to the parabelt's enhanced response, relative to area A1, to
603 harmonic sounds with varying degrees of temporal coherence across frequency channels, termed
604 "auditory figure ground" stimuli (Schneider et al., 2018). Across studies of the cortical hierarchy,
605 there appears to be a notable reduction in response to simple stimuli, such as tones, and an
606 increase in selectivity for complex stimuli with characteristics, e.g. low modulation frequencies.
607 This likely underpins enhanced selectivity for species-specific communication sounds, and
608 associated visual stimuli, as one ascends the hierarchy (Mackey et al., 2024b).
609
610 *Previous laminar studies.* The results presented here provide the first study of AM encoding
611 utilizing laminar resolution at multiple levels across the NHP auditory cortical hierarchy.
612 Previous laminar studies in cat primary auditory cortex found that the extragranular layers
613 preferentially encode slower AM relative to the thalamorecipient granular layer (Atencio and
614 Schreiner, 2010), and that spectrotemporal feature selectivity is hierarchical i.e. Granular >
615 Supragranular > Infragranular (Atencio et al., 2009). This is consistent with what we observed
616 for MUA in core primary AC, though interestingly this trend was much less apparent in the
617 parabelt (Figure 3 E-H). Murine studies have suggested robust differences in spectrotemporal
618 tuning between layer 5 and layer 6 neurons, with L5 being sluggish relative to L6, and exhibiting
619 much broader, less sparse tuning to spectral and temporal sound features (Williamson and
620 Polley, 2019). Our measures of local population activity (CSD and MUA) are likely integrating
621 across these populations, so, perhaps unsurprisingly, we did not see a bimodal distribution
622 (reflecting L5 and L6 units) in infragranular AM encoding measures. However, the robust AM
623 encoding in infragranular populations are consistent with these previous data on L6 units. These
624 studies, in combination with the present report, describe some of the only data on the
625 intracortical circuits underlying temporal sound envelope encoding in auditory cortex. The
626 present report now builds on this knowledge by quantifying laminar-resolved AM encoding in
627 the NHP parabelt.
628
629 *Task engagement*. Though the NHPs in the present report were not engaged in a task, previous
630 studies have suggested that stimulus complexity and task relevance exert substantial influence on
631 stimulus responses, particularly in nonprimary cortical areas. In secondary and tertiary auditory

632 cortices of ferrets (the dorsal posterior ectosylvian gyrus, and rostral ventral posterior auditory
633 field, respectively), hierarchical differences, such as the progressive influence of task-related
634 factors, have been well-studied (Atiani et al., 2014; Elgueda et al., 2019). A similar hierarchical
635 progression is present between primary and secondary auditory cortex of NHPs discriminating
636 AM noise, namely, single-unit discriminability via rate and temporal codes are enhanced by task-
637 engagement (Niwa et al., 2015). Entrainment to rhythmic stimuli also appears to be behaviorally-
638 gated in this same sense (O'Connell et al., 2015). Thus, if our NHPs had been engaged in a task,
639 particularly one that indexed AM feature discrimination, we would expect enhanced encoding
640 relative to what we report here.
641
642 *Decoding studies.* Previous decoding studies offer insight into the present results (Downer et al.,
643 2021; Tovar et al., 2020). Tovar et al. (2020) leveraged multivariate pattern analysis across
644 channels to reveal that orientation information is relatively well preserved across all layer
645 compartments in V1, and eye-of-origin information decreases in the infragranular layers. Tovar
646 et al. also noted that repetition suppression, which is greatest in the extragranular layers,
647 contributed to their enhanced decoding of stimulus repetition. This may be analogized to our
648 results, where the granular layer often exhibited the greatest mutual information about different
649 modulation frequencies, likely due to its rapid response characteristics. Though this pattern was
650 most notable in area A1, and the parabelt displayed a less clear granular > supragranular >
651 infragranular gradient in AM encoding. Another study that utilized decoding analysis that is
652 relevant to the present results is Downer et al. (2021). Downer et al. utilized decoding analyses
653 on simulated and empirical neuronal populations from single-unit recordings, and revealed
654 robust population-level synchronization to a wide range of modulation frequencies, 4-512 Hz
655 (Downer et al., 2021). This is consistent with our MUA measures in area A1. Both studies
656 suggest code-agnostic measures (e.g. linear discriminant analysis in the present report) on local
657 population responses can reveal information not readily apparent in single-unit measures using
658 phase-locking or an average rate code. Such code-agnostic measures also avoid commonly noted
659 problems with vector strength and the Rayleigh test for synchrony, namely potential for false
660 discoveries (Yin et al., 2011), and parametric statistical assumptions (Kajikawa and Hackett,
661 2005).
662

Interhemispheric differences. Our analysis demonstrates similar hierarchical and inter-hemispheric differences to human subjects in Boemio et al. (2005), and our results resemble previous NHP studies demonstrating sound-driven hemispheric asymmetries (left hemisphere enhancement) in the lateral sulcus, and the extent of the superior temporal gyrus, including the temporal pole (Poremba et al., 2003, 2004). Our results suggest the supragranular layers are the main contributing layer to the left-hemisphere dominance in encoding a wide range of temporal fluctuations (1.6-200 Hz), which aligns with other studies which defined supragranular sources potentially underlying noninvasive measures in fMRI, EEG, and MEG studies (e.g. (Kajikawa et al., 2024; Lakatos et al., 2020; Leszczyński et al., 2020; Peterson et al., 1995)). Additionally, a previous NHP study has similarly demonstrated enhanced entrainment of low frequency (~1.6 Hz) oscillations in left, relative to right, supragranular A1, which corroborates our results (O'Connell et al., 2015).

REFERENCES

Atencio, C.A., and Schreiner, C.E. (2010). Laminar diversity of dynamic sound processing in cat primary auditory cortex. J. Neurophysiol. *103*, 192–205.

Atencio, C.A., Sharpee, T.O., and Schreiner, C.E. (2009). Hierarchical computation in the canonical auditory cortical circuit. Proc. Natl. Acad. Sci. U. S. A. *106*, 21894–21899.

Atiani, S., David, S. V., Elgueda, D., Locastro, M., Radtke-Schuller, S., Shamma, S.A., and Fritz, J.B. (2014). Emergent Selectivity for Task-Relevant Stimuli in Higher-Order Auditory Cortex. Neuron *82*, 486–499.

Banno, T., Shirley, H., Fishman, Y.I., and Cohen, Y.E. (2023). Changes in neural readout of response magnitude during auditory streaming do not correlate with behavioral choice in the auditory cortex. Cell Rep. *42*, 113493.

Benjamini, Y., and Hochberg, Y. (1995). Controlling the false discovery rate: a practical and powerful approach to multiple testing. J. R. Stat. Soc. Ser. B *57*, 289–300.

Boemio, A., Fromm, S., Braun, A., and Poeppel, D. (2005). Hierarchical and asymmetric temporal sensitivity in human auditory cortices. Nat. Neurosci. *8*, 389–395.

Camalier, C.R., D'Angelo, W.R., Sterbing-D'Angelo, S.J., de la Mothe, L.A., and Hackett, T.A.

(2012). Neural latencies across auditory cortex of macaque support a dorsal stream supramodal timing advantage in primates. Proc. Natl. Acad. Sci. *109*, 18168–18173.

Dheerendra, P., Baumann, S., Joly, O., Balezeau, F., Petkov, C.I., Thiele, A., and Griffiths, T.D. (2021). The Representation of Time Windows in Primate Auditory Cortex. Cereb. Cortex 1–13.

Ding, N., Patel, A.D., Chen, L., Butler, H., Luo, C., and Poeppel, D. (2017). Temporal modulations in speech and music. Neurosci. Biobehav. Rev. *81*, 181–187.

Downer, J.D., Niwa, M., and Sutter, M.L. (2017). Hierarchical differences in population coding within auditory cortex. J. Neurophysiol. *118*, 717–731.

Downer, J.D., Bigelow, J., Runfeldt, M.J., and Malone, B.J. (2021). Temporally precise population coding of dynamic sounds by auditory cortex. J. Neurophysiol. *126*, 148–169.

Elgueda, D., Duque, D., Radtke-schuller, S., Yin, P., David, S. V., Shamma, S.A., and Fritz, J.B. (2019). State-dependent encoding of sound and behavioral meaning in a tertiary region of the ferret auditory cortex. Nat. Neurosci. *22*.

Fishman, Y.I., Reser, D.H., Arezzo, J.C., and Steinschneider, M. (2001). Neural correlates of auditory stream segregation in primary auditory cortex of the awake monkey. *151*, 167–187.

Fishman, Y.I., Arezzo, J.C., and Steinschneider, M. (2004). Auditory stream segregation in monkey auditory cortex: effects of frequency separation, presentation rate, and tone duration. J. Acoust. Soc. Am. *116*, 1656–1670.

Freeman, J.A., and Nicholson, C.H. (1975). Experimental optimization of current source-density technique for anuran cerebellum. J. Neurophysiol. *38*, 369–382.

Fries, P., and Maris, E. (2022). What to do if N is two? J. Cogn. Neurosci. *34*, 1114–1118.

Hackett, T.A., Stepniewska, I., and Kaas, J.H. (1998). Prefrontal connections of the parabelt auditory cortex in macaque monkeys. J. Comp. Neurol. *400*, 271–286.

Hackett, T.A., Preuss, T.M., and Kaas, J.H. (2001). Architectonic identification of the core region in auditory cortex of macaques, chimpanzees, and humans. J. Comp. Neurol. *441*, 197–222.

Hackett, T.A., de la Mothe, L.A., Camalier, C.R., Falchier, A., Lakatos, P., Kajikawa, Y., and Schroeder, C.E. (2014). Feedforward and feedback projections of caudal belt and parabelt areas of auditory cortex: Refining the hierarchical model. Front. Neurosci. *8*, 1–21.

Hamilton, L.S., Oganian, Y., Hall, J., and Chang, E.F. (2021). Parallel and distributed encoding of speech across human auditory cortex. Cell 1–14.

Henry, K.S., Neilans, E.G., Abrams, K.S., Idrobo, F., and Carney, L.H. (2016). Neural correlates of behavioral amplitude modulation sensitivity in the budgerigar midbrain. J. Neurophysiol. *115*, 1905–1916.

Henry, K.S., Abrams, K.S., Forst, J., Mender, M.J., Neilans, E.G., Idrobo, F., and Carney, L.H. (2017). Midbrain Synchrony to Envelope Structure Supports Behavioral Sensitivity to Single-Formant Vowel-Like Sounds in Noise. JARO - J. Assoc. Res. Otolaryngol. *18*, 165–181.

Hoglen, N.E.G., Larimer, P., Phillips, E.A.K., Malone, B.J., and Hasenstaub, A.R. (2018). Amplitude modulation coding in awake mice and squirrel monkeys. J. Neurophysiol. *119*, 1753–1766.

Johnson, J.S., Yin, P., O'Connor, K.N., and Sutter, M.L. (2012). Ability of primary auditory cortical neurons to detect amplitude modulation with rate and temporal codes: Neurometric analysis. J. Neurophysiol. *107*, 3325–3341.

Johnson, J.S., Niwa, M., O'Connor, K., Malone, B.J., and Sutter, M.L. (2024). Hierarchical emergence of opponent coding in auditory belt cortex. BioRxiv 1–37.

Joris, P.X., and Yin, T.C.T. (1992). Responses to amplitude-modulated tones in the auditory nerve of the cat. J. Acoust. Soc. Am. *91*, 215–232.

Joris, P.X., Schreiner, C.E., and Rees, A. (2004). Neural Processing of Amplitude-Modulated Sounds. Physiol. Rev. *84*, 541–577.

Kajikawa, Y., and Hackett, T.A. (2005). Entropy analysis of neuronal spike train synchrony. J. Neurosci. Methods *149*, 90–93.

Kajikawa, Y., and Schroeder, C.E. (2011). How Local Is the Local Field Potential? Neuron *72*, 847–858.

Kajikawa, Y., Frey, S., Ross, D., Falchier, A., Hackett, T.A., and Schroeder, C.E. (2015). Auditory Properties in the Parabelt Regions of the Superior Temporal Gyrus in the Awake Macaque Monkey: An Initial Survey. J. Neurosci. *35*, 4140–4150.

Kajikawa, Y., Smiley, J.F., and Schroeder, C.E. (2017). Primary generators of visually evoked field potentials recorded in the macaque auditory cortex. J. Neurosci. *37*, 10139–10153.

Kajikawa, Y., Mackey, C.A., and O'Connell, M.N. (2024). Laminar pattern of sensory-evoked

dynamic high-frequency oscillatory activity in the macaque auditory cortex. Cereb. Cortex *34*.

Lakatos, P., Pincze, Z., Fu, K.-M.G., Javitt, D.C., Karmos, G., and Schroeder, C.E. (2005a). Timing of pure tone and noise-evoked responses in macaque auditory cortex. Neuroreport *16*, 933–937.

Lakatos, P., Shah, A.S., Knuth, K.H., Ulbert, I., Karmos, G., and Schroeder, C.E. (2005b). An oscillatory hierarchy controlling neuronal excitability and stimulus processing in the auditory cortex. J. Neurophysiol. *94*, 1904–1911.

Lakatos, P., O'Connell, M.N., Barczak, A., Mills, A., Javitt, D.C., and Schroeder, C.E. (2009). The Leading Sense: Supramodal Control of Neurophysiological Context by Attention. Neuron *64*, 419–430.

Lakatos, P., Musacchia, G., O'Connel, M.N., Falchier, A.Y., Javitt, D.C., and Schroeder, C.E. (2013). The Spectrotemporal Filter Mechanism of Auditory Selective Attention Supplemental Info. Neuron *77*, 750–761.

Lakatos, P., O'Connell, M.N., Barczak, A., McGinnis, T., Neymotin, S., Schroeder, C.E., Smiley, J.F., and Javitt, D.C. (2020). The Thalamocortical Circuit of Auditory Mismatch Negativity. Biol. Psychiatry *87*, 770–780.

Langner, G., and Schreiner, C.E. (1988). Periodicity coding in the inferior colliculus of the cat. I. Neuronal mechanisms. J. Neurophysiol. *60*, 1799–1822.

Leszczyński, M., Barczak, A., Kajikawa, Y., Ulbert, I., Falchier, A.Y., Tal, I., Haegens, S., Melloni, L., Knight, R.T., and Schroeder, C.E. (2020). Dissociation of broadband high-frequency activity and neuronal firing in the neocortex. Sci. Adv. 1–13.

Lu, H., Mehta, A.H., and Oxenham, A.J. (2022). Methodological considerations when measuring and analyzing auditory steady-state responses with multi-channel EEG. Curr. Res. Neurobiol. *3*, 100061.

Mackey, C.A., Hauser, S., Schoenhaut, A.M., Temghare, N., and Ramachandran, R. (2024a). Hierarchical differences in the encoding of amplitude modulation in the subcortical auditory system of awake nonhuman primates. J. Neurophysiol. *132*, 1098–1114.

Mackey, C.A., O'Connell, M.N., Hackett, T.A., Schroeder, C.E., and Kajikawa, Y. (2024b). Laminar organization of visual responses in core and parabelt auditory cortex. Cereb. Cortex *34*.

Mehta, A.D., Ulbert, I., and Schroeder, C.E. (2000a). Intermodal selective attention in monkeys I: Distribution and timing of effects across visual areas. Cereb. Cortex *10*, 343–358.

Mehta, A.D., Ulbert, I., and Schroeder, C.E. (2000b). Intermodal selective attention in monkeys. II: physiological mechanisms of modulation. Cereb. Cortex *10*, 359–370.

Merzenich, M.M., and Brugge, J.F. (1973). Representation of the cochlear partition on the superior temporal plane of the macaque monkey. Brain Res. *50*, 275–296.

Mitzdorf, U. (1985). Current source-density method and application in cat cerebral cortex: investigation of evoked potentials and EEG phenomena. Physiol. Rev. *65*, 37–100.

Moody, D.B. (1994). Detection and discrimination of amplitude-modulated signals by macaque monkeys. J. Acoust. Soc. Am. *95*, 3499–3510.

Nelson, P.C., and Carney, L.H. (2007). Neural rate and timing cues for detection and discrimination of amplitude-modulated tones in the awake rabbit inferior colliculus. J. Neurophysiol. *97*, 522–539.

Niwa, M., O'Connor, K.N., Engall, E., Johnson, J.S., and Sutter, M.L. (2015). Hierarchical effects of task engagement on amplitude modulation encoding in auditory cortex. J. Neurophysiol. *113*, 307–327.

O'Connell, M.N., Barczak, A., Schroeder, C.E., and Lakatos, P. (2014). Layer Specific Sharpening of Frequency Tuning by Selective Attention in Primary Auditory Cortex. J. Neurosci. *34*, 16496–16508.

O'Connell, M.N., Barczak, A., Ross, D., McGinnis, T., Schroeder, C.E., and Lakatos, P. (2015). Multi-scale entrainment of coupled neuronal oscillations in primary auditory cortex. Front. Hum. Neurosci. *9*, 1–16.

Penikis, K.B., and Sanes, D.H. (2023). A redundant cortical code for speech envelope. J. Neurosci. *43*, 93–112.

Peterson, N.N., Schroeder, C.E., and Arezzo, J.C. (1995). Neural generators of early cortical somatosensory evoked potentials in the awake monkey. Electroencephalogr. Clin. Neurophysiol. Potentials Sect. *96*, 248–260.

Poremba, A., Saunder, R.C., Crane, A.M., Cook, M., Sokoloff, L., and Mishkin, M. (2003). Functional mapping of the primate auditory system. Science (80-.). *299*, 568–572.

Poremba, A., Malloy, M., Saunders, R.C., Carson, R.E., Herscovitch, P., and Mishkin, M. (2004). Species-specific calls evoke asymmetric activity in the monkey's temporal poles.

Nature *427*, 448–451.

Rauschecker, J.P. (1997). Processing of complex sounds in the auditory cortex of cat, monkey, and man. Acta Otolaryngol. *117*, 34–38.

Rhode, W.S., Roth, G.L., and Recio-spinoso, A. (2010). Response properties of cochlear nucleus neurons in monkeys. Hear. Res. *259*, 1–15.

Romanski, L.M., Tian, B., Fritz, J., Mishkin, M., Goldman-Rakic, P.S., and Rauschecker, J.P. (1999). Dual streams of auditory afferents target multiple domains in the primate prefrontal cortex. Nat. Neurosci. *2*, 1131–1136.

Rosen, S. (1992). Temporal information in speech. Phil. Trans. R. Soc. Lond. B *336*, 367–373.

Sayles, M., Füllgrabe, C., and Winter, I.M. (2013). Neurometric amplitude-modulation detection threshold in the guinea-pig ventral cochlear nucleus. J. Physiol. *591*, 3401–3419.

Schneider, F., Dheerendra, P., Balezeau, F., Ortiz-Rios, M., Kikuchi, Y., Petkov, C.I., Thiele, A., and Griffiths, T.D. (2018). Auditory figure-ground analysis in rostral belt and parabelt of the macaque monkey. Sci. Rep. *8*, 1–8.

Shi, K., Quass, G.L., Rogalla, M.M., Ford, A.N., Czarny, J.E., and Apostolides, P.F. (2024). Population coding of time-varying sounds in the nonlemniscal inferior colliculus. J. Neurophysiol. *131*, 842–864.

Steinschneider, M., Tenke, C.E., Schroeder, C.E., Javitt, D.C., Simpson, G. V, Arezzo, J.C., and Vaughan Jr, H.G. (1992). Cellular generators of the cortical auditory evoked potential initial component. Electroencephalogr. Clin. Neurophysiol. Potentials Sect. *84*, 196–200.

Steinschneider, M., Reser, D.H., Fishman, Y.I., Schroeder, C.E., and Arezzo, J.C. (1998). Click train encoding in primary auditory cortex of the awake monkey: evidence for two mechanisms subserving pitch perception. J. Acoust. Soc. Am. *104*, 2935–2955.

Tallon-Baudry, C., Bertrand, O., Delpuech, C., and Pernier, J. (1996). Stimulus Specificity of Phase-Locked and Non-Phase-Locked 40 Hz Visual Responses in Human. J. Neurosci. *16*, 4240 LP – 4249.

Tovar, D.A., Westerberg, J.A., Cox, M.A., Dougherty, K., Carlson, T.A., Wallace, M.T., and Maier, A. (2020). Stimulus Feature-Specific Information Flow Along the Columnar Cortical Microcircuit Revealed by Multivariate Laminar Spiking Analysis. Front. Syst. Neurosci. *14*, 1–14.

Wang, X., Lu, T., Bendor, D., and Bartlett, E.L. (2008). Neural coding of temporal information

in auditory thalamus and cortex. Neuroscience *154*, 294–303.

Williamson, R.S., and Polley, D.B. (2019). Parallel pathways for sound processing and functional connectivity among layer 5 and 6 auditory corticofugal neurons. Elife *8*, e42974.

Yao, J.D., and Sanes, D.H. (2021). Temporal Encoding is Required for Categorization, But Not Discrimination. Cereb. Cortex *31*, 2886–2897.

Yin, P., Johnson, J.S., O'Connor, K.N., and Sutter, M.L. (2011). Coding of amplitude modulation in primary auditory cortex. J. Neurophysiol. *105*, 582–600.

Zion Golumbic, E., Ding, N., Bickel, S., Lakatos, P., Schevon, C.A., McKhann, G.M., Goodman, R.R., Emerson, R., Mehta, A.D., Simon, J.Z., et al. (2013). Mechanisms underlying selective neuronal tracking of attended speech at a "cocktail party." Neuron *77*, 980–991.